Identifying topological order via unsupervised machine learning

Joaquin F. Rodriguez-Nieva^{1,*} and Mathias S. Scheurer^{1,†}
¹Department of Physics, Harvard University, Cambridge MA 02138, USA

Machine learning of topological phase transitions has proven to be challenging due to their inherent non-local nature. We propose an unsupervised approach based on diffusion maps that learns topological phase transitions from raw data without the need of manual feature engineering. Using bare spin configurations as input, the approach is shown to be capable of classifying samples of the two-dimensional XY model by winding number and capture the Berezinskii-Kosterlitz-Thouless transition. We also discuss a connection between the output of diffusion maps and the eigenstates of a quantum-well Hamiltonian.

Introduction. — Machine learning techniques [1–3] are exquisitely tailored to uncover structure in complex data and to efficiently describe it with a minimal number of parameters. Recent advances in this field, demonstrated in areas as diverse as computer vision and natural language processing, have motivated the application of machine learning to various problems in condensed matter physics, with the hope of mutual benefits. Of the many conceptually and practically valuable applications [4–11], using machine learning to classify phases of matter and describe phase transitions has taken center stage [12–33]. While many conventional, symmetry-breaking, phase transitions can be efficiently captured by machine learning approaches due to the local nature of the order parameter, topological phase transitions are particularly difficult to "learn" [25]. The difficulty stems from the fact that topological phase transitions are characterized by the proliferation of non-local, topological defects that are suppressed in the topologically ordered phase [34, 35].

One common machine learning approach which is used to classify phases of matter, either topological or nontopological, is based on supervised methods. These require prior labeling of the states (i.e., the input data) in well-known regimes, e.g., whether a state belongs to a ferro- or paramagnetic phase [12]. The supervised step, however, assumes prior knowledge of the underlying phases of the system and, as such, this approach rules out the possibility of learning unknown phases. Contrary to the supervised case, unsupervised methods learn structure from the data itself without the need of prior labeling. As a result, unsupervised machine learning is particularly useful when the classification (or its mere existence) is not known a priori.

Here we present an unsupervised machine learning approach that can efficiently classify states according to their topological properties without knowledge of the underlying topological invariant, and can detect topological phase transitions from raw data. The approach is based on dimensional reduction via diffusion maps [36–38], which has been used for speaker identification [39] or face recognition [40], and very naturally implements the notion of homotopy by construction of a diffusion process on the data set, see Fig. 1. To demonstrate the algorithm,

we show that it can efficiently learn the global, topological aspects of the Berezinskii-Kosterlitz-Thouless (BKT) phase transition [34, 41–43], which has proven to be notoriously difficult with other machine learning techniques: as discussed in detail in Ref. 25, significant feature engineering, such as using vorticity as input, is required to learn the BKT transition rather than the magnetization of finite samples [26–33].

Winding number and diffusion maps. — To introduce the method, let us consider one of the simplest examples of a topological invariant, the winding number ν associated with continuous mappings $S_1 \rightarrow S_1$ between two one-spheres: $\theta \in [0, 2\pi) \to \mathbf{S}(\theta) \in \mathbb{R}^2$ with $\mathbf{S}^2 = 1$ and $S(0) = S(2\pi)$. The winding number $\nu \in \mathbb{Z}$ is given by the number of times the unit vector S winds around upon traversing S_1 , and is a topological invariant because it cannot be changed by continuous deformations of the mapping. The winding number plays a crucial role in various contexts, such as the classification of topological band insulators [44] and superconductors [45], or as the topological invariant associated with a non-contractible loop of the quasi-long-range-ordered phase of the XY model on a torus [34]. Rather than learning ν in a supervised way as recently done in Ref. 20, here we address

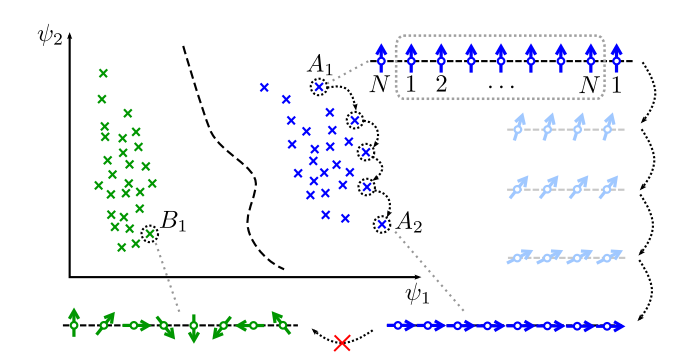


Figure 1. Topological classification using sample connectivity. Shown are samples of N classical XY spins, with periodic boundary conditions and winding numbers $\nu=0,1$, projected on a two-dimensional feature space $\psi_{1,2}$. A diffusion map clusters samples which are connected via continuous deformations, such as A_1 and A_2 , but not A_1 and B_1 .

the unsupervised version of the problem: classifying different samples of the mapping $S_1 \to S_1$ without providing the labels ν for each sample, or the number of distinct ν which are present in the data set.

To treat the problem numerically, we discretize [46] the mapping $\mathbf{S}_i = \mathbf{S}(2\pi i/N)$, i = 1, ..., N, which can be viewed as a one-dimensional (1D) chain of N classical XY spins with periodic boundary conditions, see Fig. 1. We consider m samples of XY spin configurations, which we denote $x_l = \{\mathbf{S}_i^{(l)}\}, l = 1, ..., m$. To define the notion of similarity between samples l and l', we use a function of the Euclidean norm, for instance the Gaussian kernel

$$K_{\epsilon}(x_l, x_{l'}) = \exp\left(-\frac{||x_l - x_{l'}||^2}{2N\epsilon}\right),\tag{1}$$

with variance controlled by ϵ . In the 1D XY model, the Euclidean distance between x_l and $x_{l'}$ is given by $||x_l - x_{l'}||^2/(2N) = 1 - \frac{1}{N} \sum_{i=1}^N \boldsymbol{S}_i^{(l)} \cdot \boldsymbol{S}_i^{(l')}$. As a result, Eq. (1) quantifies the similarity between two samples by local comparison of their degrees of freedom such that $K_{\epsilon}(x_l, x_{l'}) \simeq 1$ if $x_{l'}$ is a small deformation of x_l .

Importantly, Eq. (1) illustrates why unsupervised classification of topologically distinct mappings is a challenging task for conventional cluster algorithms, such as kmeans, without a priori knowledge of the explicit form of the topological invariant. In particular, two topologically equivalent samples, such as A_1 and A_2 in Fig. 1, can be equally separated from each other in Euclidean space as two topologically distinct samples, such as A_1 and B_1 in Fig. 1, i.e., $K_{\epsilon}(x_{A_1}, x_{A_2}) = K_{\epsilon}(x_{A_1}, x_{B_1}) = e^{-1/\epsilon}$. Rather than learning from local similarity between individual samples, our goal is to learn from the *qlobal con*nectivity of the entire sample space. Quantifying connectivity of samples is the essence of diffusion maps, first introduced by Coifman et al. [36] for manifold learning and dimensional reduction. Here we extend the applicability of this method to perform topological classification of phases of matter.

A diffusion map is obtained by constructing a diffusion process on the data set $X = \{x_l | l = 1, ..., m\}$. The one-step transition probability $P_{l,l'}$ from sample l to sample l' is defined as

$$P_{l,l'} = \frac{K_{\epsilon}(x_l, x_{l'})}{z_l}, \quad z_l = \sum_{l'=1}^m K_{\epsilon}(x_l, x_{l'}),$$
 (2)

where z_l has been introduced to account for probability conservation, $\sum_{l'} P_{l,l'} = 1$. The value of z_l quantifies the effective coordination number of sample l. Crucially, $P_{l,l'}$ and $K_{\epsilon}(x_l, x_{l'})$ in Eq. (1) only contain information about the local structure of the data. However, the transition probabilities $(P^t)_{l,l'}$ after many $t \in \mathbb{N}$ diffusion steps experience the global structure of the samples.

More explicitly, the "diffusion distance" between sam-

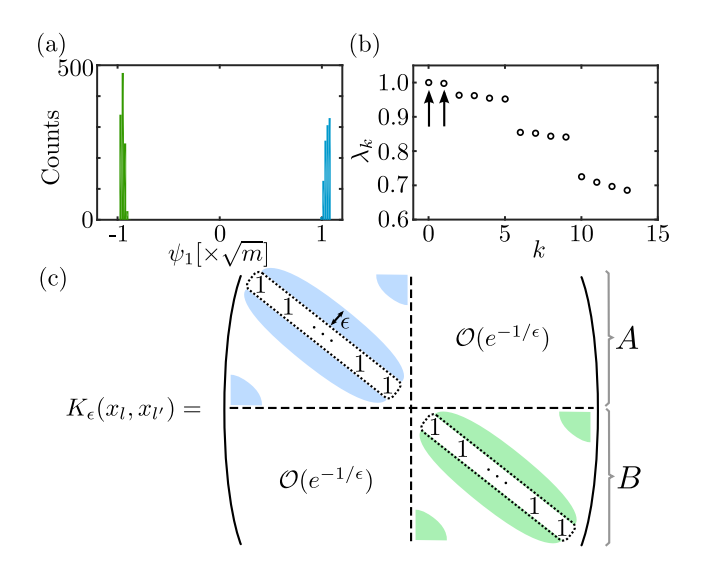


Figure 2. (a) Clustering of the first component of the diffusion map, $(\psi_1)_l$, according to winding number. Shown is a color-coded histogram of $(\psi_1)_l$, where the color code indicates the (hidden) winding number associated to each bar. (b) Largest eigenvalues of the transition probability matrix, $P_{l,l'}$ in Eq. (2). The two-fold degeneracy of the largest eigenvalue (indicated with arrows) signals the presence of two topologically distinct sectors. (c) Schematics of K_{ϵ} in Eq. (1) showing connectivity between samples for a given ϵ and two topological sectors A and B. Parameters used in (a)-(b): m = 2100, N = 64, $\sigma_{\theta} = \pi/5$.

ples l and l' after 2t times steps can be defined as

$$D_t(l, l') := \sum_{l''} \frac{1}{z_{l''}} \left[(P^t)_{l, l''} - (P^t)_{l', l''} \right]^2 \ge 0.$$
 (3)

The value of $D_t(l, l')$ is small (large) if there are many (very few) strong paths of length 2t connecting the two samples, like in case of A_1 and A_2 (A_1 and B_1) in Fig. 1. The notion of the diffusion distance motivates the introduction of the diffusion map, defined as the mapping

$$x_l \to \Phi_l := [(\psi_1)_l, (\psi_2)_l, \dots, (\psi_{m-1})_l].$$
 (4)

Here ψ_k are the right eigenvectors of the transition matrix $P\psi_k = \lambda_k \psi_k$, $k = 0, 1, \dots m - 1$, with eigenvalues $0 \le \lambda_k \le 1$, and which we order such that $\lambda_k \ge \lambda_{k+1}$. The diffusion distance (3) then becomes the weighted Euclidean norm:

$$D_t(l, l') = ||\mathbf{\Phi}_l - \mathbf{\Phi}_{l'}||_t^2 = \sum_{k=1}^{m-1} \lambda_k^{2t} [(\psi_k)_l - (\psi_k)_{l'}]^2. \quad (5)$$

Here we dropped the k=0 component because it is constant $[(\psi_0)_l=1/\sqrt{m},\ \lambda_0=1]$ and does not contribute to Eq. (5). Because of the weights λ_k^{2t} in Eq. (5), the long-time $t\to\infty$ (or global) properties of the samples is encoded in the first few $(\psi_k)_l$ components with largest λ_k . These few components, which are expected to be

similar for samples within the same topological sector in order to make $D_t(l, l')$ small, can be used for dimensional reduction and topological classification, as verified next.

Returning to the mapping $S_1 \to S_1$, we use randomly generated samples $S_i^{(l)} = (\cos \theta_i^{(l)}, \sin \theta_i^{(l)})^T$, with

$$\theta_i^{(l)} = 2\pi\nu^{(l)}i/N + \delta\theta_i^{(l)} + \bar{\theta}^{(l)}.$$
 (6)

Here $\delta\theta_i^{(l)}$ accounts for spin fluctuations at position i, which are taken from a Gaussian distribution with standard deviation σ_{θ} , $\bar{\theta}^{(l)}$ is a random number that represents global rotations, and we use m=2100. For now, let us consider having two topological sectors (or winding numbers) in our samples, $\nu^{(l)} \in \{0,1\}$, which are chosen randomly with equal probability (below we discuss the case with more topological sectors). Figure 2(a) shows the histogram of $(\psi_1)_l$ corresponding to the leading component of the diffusion map [47]. As anticipated, samples with the same ν have a similar $(\psi_1)_l$ component. Indeed, we find that $(\psi_1)_l \simeq +1/\sqrt{m} \ [(\psi_1)_l \simeq -1/\sqrt{m}]$ for $\nu=1$ $(\nu=0)$ and, as such, $(\psi_1)_l$ clusters samples by winding number.

For a generic classification problem, the main challenge is that the number n of topological sectors present in the data is not known a priori. Further, it is unlikely that $(\psi_1)_l$ alone is sufficient for classification. We argue that the answer to both problems lies in the eigenvalue spectrum λ_k . In particular, we find that n, and the resulting number of $(\psi_k)_l$ components to be considered for classification, is determined by the degeneracy of the largest eigenvalues $\lambda_k = 1$. For example, as shown in Fig. 2(b), there are two degenerate eigenvalues $\lambda_{0,1} = 1$ corresponding to the two winding numbers $\nu = 0, 1$, with a clear gap to the subleading $\lambda_{k\geq 2}$. As $\psi_0 = \text{const.}$, the topological classification can be done with ψ_1 alone in the simple case above.

The degeneracy of the largest eigenvalues can be understood from the structure of the matrix K illustrated in Fig. 2(c) upon conveniently reordering the samples by topological sector and increasing value of $\bar{\theta}^{(l)}$ (this does not affect the spectrum of λ_k and assumes a small σ_{θ} such that topological sectors are well-defined). As the two topologically distinct sectors, A and B, only couple via exponentially small matrix elements $\sim e^{-1/\epsilon}$, probability conservation in each topological sector separately, $\sum_{l'\in A} P_{l,l'} \simeq 1 - \mathcal{O}(me^{-1/\epsilon})$, ensures the existence of an eigenvalue $\lambda_k \simeq 1 - \mathcal{O}(e^{-1/\epsilon})$ up to corrections which can be made exponentially small with increasing sampling size (see Supplement S.1). For instance, in the XY model, the typical angle difference between a sample and its closest topologically connected samples is $\delta \bar{\theta} \sim 2\pi/m_{\nu}$, where m_{ν} is the number of samples within each topological sector. This gives rise to a kernel amplitude of $K_{\epsilon} \sim e^{-(2\pi/m_{\nu})^2/\epsilon}$, thus defining a scale $\epsilon \sim \epsilon_0 = \sqrt{2\pi/m_{\nu}}$ which decreases $\propto 1/\sqrt{m}$ with sampling size.

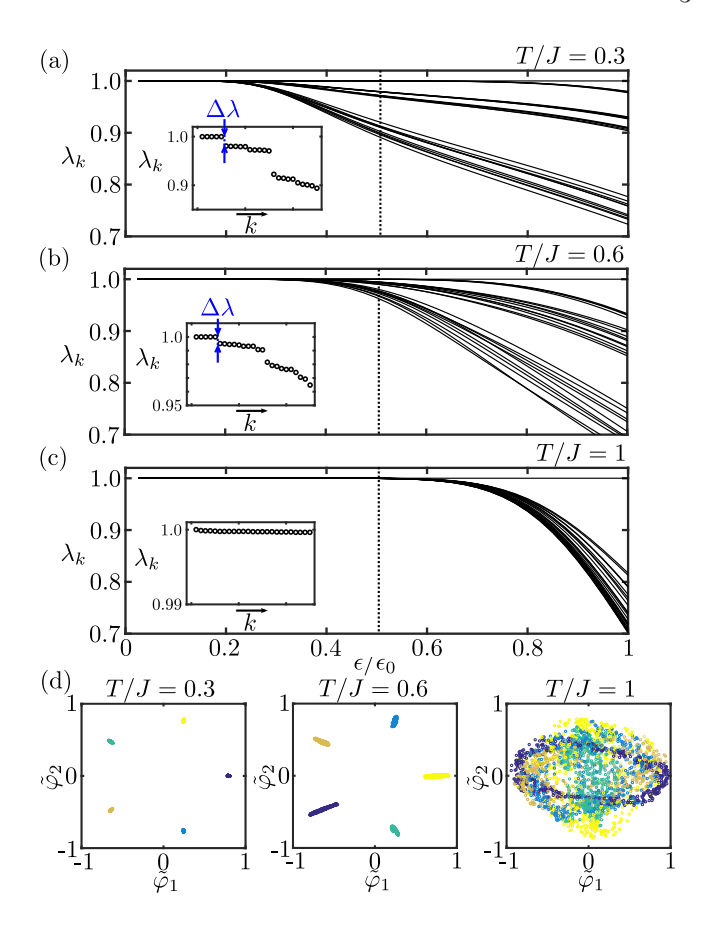


Figure 3. Largest eigenvalues $\lambda_{k\leq 24}$ of $P_{l,l'}$ as a function of ϵ for (a) T/J=0.3, (b) T/J=0.6, and (c) T/J=1.0. The insets show λ_k for $\epsilon/\epsilon_0=0.5$. (d) Projection of the 4-dimensional reduced feature space, Eq. (7), on a two-dimensional plane. The color code refers to the winding number of each sample. Parameters used are described in the main text.

With these observations in mind, we define a reduced (n-1)-dimensional $(n \ll m)$ feature space φ given by

$$x_l \to \varphi_l = [(\psi_1)_l, (\psi_2)_l, \dots, (\psi_{n-1})_l],$$
 (7)

where n is the degeneracy of the largest eigenvalue, indicating the presence of n topological sectors in sample space. From this low-dimensional feature space, it is straightforward to apply standard clustering algorithms such as k-means (see Supplement S.2). To illustrate how this general procedure is applied to a specific problem, we now consider the two-dimensional (2D) XY model.

2D XY model. — The configuration energy of the 2D XY model is given by

$$E(\{\theta_i\}) = -J \sum_{\langle i,j \rangle} \cos(\theta_i - \theta_j), \tag{8}$$

where θ_i is the angle of the XY spin at site *i* on a square lattice, $\langle i, j \rangle$ denotes summation over nearest neighbors, and we use periodic boundary conditions. This model

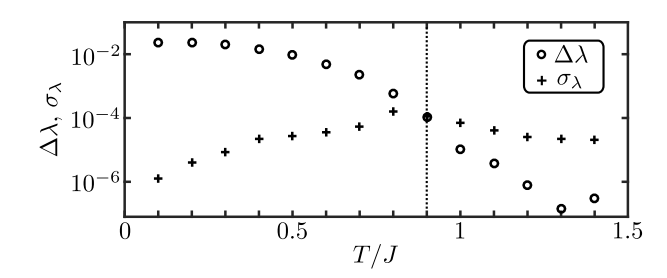


Figure 4. Unsupervised learning of the topological phase transition (dotted line). Here we exploit the failure of the algorithm to identify the n topological sectors, which leads to a transition temperature of $T_c/J=0.90\pm0.05$. The values of $\sigma_{\lambda}({\rm crosses})$ indicate the dispersion of the largest n eigenvalues, which are degenerate as $T\to 0$, and $\Delta\lambda$ (circles) is the gap with respect to the first non-degenerate eigenvalue.

exhibits the BKT transition [34, 41–43] at the critical temperature $T_c/J \simeq 0.89$ [48]: in the topologically ordered phase, $T < T_c$, free vortices are suppressed and two winding numbers, ν_x and ν_y along the x and y direction, can be defined [34] to classify globally distinct metastable states. The presence of free vortices at $T \geq T_c$ render these invariants ill-defined, which is the hallmark of the BKT transition.

To feed the algorithm, we use spin configurations on a square lattice with $N=32\times 32$ sites, governed by the thermal distribution $\rho(\{\theta_i\})\propto e^{-E(\{\theta_i\})/T}$, and sample over different topological sectors. Specifically, we allow for five possible winding numbers, $(\nu_x,\nu_y)=(0,0),(1,0),(0,1),(-1,0),(0,-1)$ with $m_{\nu}=500$ samples each, and use the Metropolis algorithm with local updates in order to thermalize our samples to temperature T. The m=2500 samples are then shuffled and winding number labels are hidden and stored for later comparison with the output of the diffusion map.

Figure 3(a)-(c) shows the eigenvalues λ_k of $P_{l,l'}$ as function of ϵ , and for increasing values of T. The degeneracy of the largest eigenvalue (as $\epsilon \to 0$) signals the number of topological sectors: we find n=5 in Fig. 3(a)-(b), and n=1 in Fig. 3(c). The failure of the algorithm to identify the five different topological sectors at T/J=1 is a smoking gun of the topological phase transition.

To illustrate the fidelity of the clustering below T_c , we project the low-dimensional feature space φ , Eq.(7), into a two-dimensional plane, $(\tilde{\varphi}_k)_l = \sum_{k'=1}^{n-1} a_{k,k'} (\varphi_{k'})_l$, k=1,2, with $a_{k,k'}$ chosen so as to maximize the visibility of clusters. As can be seen in Fig. 3(d), the algorithm exhibits 100% fidelity in the classification for $T < T_c$, even for our moderate sampling size and temperatures approaching T_c .

Learning the topological phase transition. — The failure of the clustering algorithm to identify different topological sectors can be used as diagnostics of a topolog-

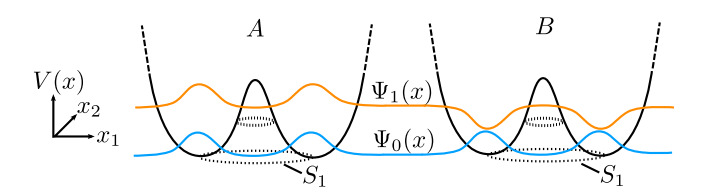


Figure 5. Illustration of the diffusion map in the continuum limit. Shown are the degenerate ground states Ψ_0 and Ψ_1 in the case of two topologically distinct sectors, A and B, which correspond to the minima of the potential V(x), see Eq.(9).

ical phase transition. Deviations from the n-fold degeneracy of the largest eigenvalue, quantified by $\sigma_{\lambda} = \frac{1}{n} \sum_{k=0}^{n-1} (\lambda_k - \bar{\lambda})^2$ with $\bar{\lambda} = \frac{1}{n} \sum_{k=0}^{n-1} \lambda_k$, measures the probability of creating vortex-antivortex pairs and tunneling between topological sectors. As such, to determine the T_c , we compare σ_{λ} with the gap $\Delta \lambda = \lambda_n - \lambda_{n-1}$. Using this criterion, we find that the topological phase transition occurs at $T/J = 0.90 \pm 0.05$, see Fig. 4, which is in agreement with the known value of T_c/J for our system size [25]. Further, we checked that the clustering fails precisely at this value, see Fig. 3(d) and extended version in Supplement S.3.

Diffusion maps in the continuum limit. — At low temperatures, the output of the diffusion map, $(\psi_k)_l$ and λ_k , can be understood in terms of the eigenstates Ψ_k and eigenvalues E_k of a many-body quantum-well Hamiltonian. Let us first focus on a single topological sector, and take $m \to \infty$. In this limit, the summations over sample space can be interpreted as Monte Carlo approximations of integrals, e.g., $z_l \sim z(x_l) = \int_{\mathcal{C}} \mathrm{d}x' K(x_l, x') \rho(x')$ in Eq. (2), where x' is integrated over configuration space \mathcal{C} , with a probability distribution $\rho(x') \propto e^{-E(x')/T}$ and energy E(x'). It was shown in Ref. 38 that, for small ϵ , the eigenvectors and eigenvalues of $P_{l,l'}$ can be written as $(\psi_k)_l \sim \Psi_k(x_l)/\rho(x_l)$ and $\lambda_k \sim 1 - \epsilon E_k$, where Ψ_k and E_k are the eigenstates and energies of

$$\hat{\mathcal{H}} = \frac{\hat{p}^2}{2} + V(x), \quad V(x) = \frac{||\nabla_x E||^2}{2T^2} - \frac{\Delta_x E}{2T}.$$
 (9)

Here $\hat{\boldsymbol{p}} = -i\nabla_x$ is the momentum operator, ∇_x is the gradient on \mathcal{C} , and $\Delta_x = \nabla_x \cdot \nabla_x$ is the Laplacian. For instance, in the XY model in Eq. (8), we have $\mathcal{C} = \mathbf{S}_1^N$ and $\hat{\boldsymbol{p}} = -i(\partial_{\theta_1}, \dots, \partial_{\theta_N})$. As illustrated in Fig. 5, V(x) resembles a quantum well with the minima occurring on a submanifold of \mathcal{C} where E is minimized. Crucial for topological classification is the existence of the "zero mode" $\Psi_0(x) = \rho(x)$ of $\hat{\mathcal{H}}$, i.e., with $E_0 = 0$ (or $\lambda_0 = 1$).

In the presence of, say, two topological sectors, A and B, each of which provides a zero mode, there will be a two-fold degeneracy $E_{0,1}=0$ ($\lambda_{0,1}=1$). In this case, the quantum system resembles a double quantum well, see Fig. 5, with high potential barriers and exponentially small tunneling coupling. The two-fold degener-

ate ground state will be formed by an even (k=0) and an odd (k=1) eigenstate with exponentially small splitting (see Supplement S.1): $\Psi_0(x) = \rho(x)$, $\Psi_1(x) = \rho(x)$ if $x \in A$, and $\Psi_1(x) = -\rho(x)$ if $x \in B$. As a result, the sign of the antisymmetric state $\Psi_1(x)$ encodes the topological sector of x, as we have seen in Fig. 2(a). Extending this argument to n topological sectors with n zero modes is straightforward.

We finally point out that, at low T, the excited state spectrum encodes the submanifold in which the (quasi)long range order parameter lives: as $T \to 0$, Eq. (9) effectively solves the Laplacian on the submanifold of \mathcal{C} where V is minimal. For instance, in the XY model, the first excited states of $\hat{\mathcal{H}}$ are well approximated by the eigenvalues of Δ_x on S_1 , i.e. $E_k = k^2/2$, non-degenerate for k = 0, and two-fold degenerate for $k \geq 1$ [see λ_k in Fig. 2(b) and in insets of Figs. 3(a)-(c)].

Conclusion. — We have shown that diffusion maps can be used for topological classification and to learn topological phase transitions in an unsupervised fashion. The success of this approach on learning the BKT transition suggests that diffusion maps can complement other versatile machine learning methods, such as those based on neural networks, in order to perform fully unsupervised studies of exotic phases of matter.

We thank Shubhayu Chatterjee, Peter P. Orth, Hannes Pichler, Subir Sachdev, and Yi-Zhuang You for useful discussions. JFRN acknowledges support from the Harvard-MIT Center of Ultracold Atoms (CUA). MS acknowledges support from the German National Academy of Sciences Leopoldina through grant LPDS 2016-12.

- * jrodrigueznieva@fas.harvard.edu
- † mscheurer@g.harvard.edu
- [1] M. A. Nielsen, Neural Networks and Deep Learning (Determination Press, 2015).
- [2] I. Goodfellow, Y. Bengio, and A. Courville, Deep Learning (MIT Press, 2016) http://www.deeplearningbook.org.
- [3] P. Mehta, M. Bukov, C.-H. Wang, A. G. Day, C. Richardson, C. K. Fisher, and D. J. Schwab, arXiv:1803.08823 (2018).
- [4] P. Mehta and D. J. Schwab, arXiv:1410.3831 (2014).
- [5] G. Carleo and M. Troyer, Science **355**, 602 (2017).
- [6] D.-L. Deng, X. Li, and S. D. Sarma, arXiv:1609.09060 (2016).
- [7] J. Liu, Y. Qi, Z. Y. Meng, and L. Fu, Phys. Rev. B 95, 041101 (2017).
- [8] G. Torlai, G. Mazzola, J. Carrasquilla, M. Troyer,
 R. Melko, and G. Carleo, Nature Physics (2018),
 10.1038/s41567-018-0048-5.
- [9] Y.-Z. You, Z. Yang, and X.-L. Qi, Phys. Rev. B 97, 045153 (2018).
- [10] G. Carleo, Y. Nomura, and M. Imada, arXiv:1802.09558

- (2018).
- [11] S. Spillard, C. J. Turner, and K. Meichanetzidis, arXiv:1803.01035 (2018).
- [12] J. Carrasquilla and R. G. Melko, Nature Physics 13, 431 (2017).
- [13] K. Ch'ng, J. Carrasquilla, R. G. Melko, and E. Khatami, Phys. Rev. X 7, 031038 (2017).
- [14] Y. Zhang and E.-A. Kim, Phys. Rev. Lett. 118, 216401 (2017).
- [15] Y. Zhang, R. G. Melko, and E.-A. Kim, Phys. Rev. B 96, 245119 (2017).
- [16] E. P. L. van Nieuwenburg, Y.-H. Liu, and S. D. Huber, Nature Physics 13, 435 EP (2017).
- [17] T. Ohtsuki and T. Ohtsuki, Journal of the Physical Society of Japan 85, 123706 (2016).
- [18] T. Ohtsuki and T. Ohtsuki, Journal of the Physical Society of Japan 86, 044708 (2017).
- [19] N. Yoshioka, Y. Akagi, and H. Katsura, arXiv:1709.05790 (2017).
- [20] P. Zhang, H. Shen, and H. Zhai, Phys. Rev. Lett. 120, 066401 (2018).
- [21] D. Carvalho, N. A. García-Martínez, J. L. Lado, and J. Fernández-Rossier, Phys. Rev. B 97, 115453 (2018).
- [22] P. Huembeli, A. Dauphin, and P. Wittek, Phys. Rev. B 97, 134109 (2018).
- [23] I. Iakovlev, O. Sotnikov, and V. Mazurenko, arXiv:1803.06682 (2018).
- [24] R. A. Vargas-Hernández, J. Sous, M. Berciu, and R. V. Krems, arXiv:1803.08195 (2018).
- [25] M. J. S. Beach, A. Golubeva, and R. G. Melko, Phys. Rev. B 97, 045207 (2018).
- [26] C. Wang and H. Zhai, arXiv:1803.01205 (2018).
- [27] W. Hu, R. R. P. Singh, and R. T. Scalettar, Phys. Rev. E 95, 062122 (2017).
- [28] S. J. Wetzel, Phys. Rev. E **96**, 022140 (2017).
- [29] C. Wang and H. Zhai, Phys. Rev. B 96, 144432 (2017).
- [30] M. Cristoforetti, G. Jurman, A. I. Nardelli, and C. Furlanello, arXiv:1705.09524 (2017).
- [31] P. Broecker, F. F. Assaad, and S. Trebst, arXiv:1707.00663 (2017).
- [32] W. Zhang, J. Liu, and T.-C. Wei, arXiv:1804.02709 (2018).
- [33] P. Suchsland and S. Wessel, arXiv:1802.09876 (2018).
- [34] J. M. Kosterlitz and D. J. Thouless, Journal of Physics C: Solid State Physics 6, 1181 (1973).
- [35] S. Sachdev, arXiv:1801.01125 (2018).
- [36] R. R. Coifman, S. Lafon, A. B. Lee, M. Maggioni, B. Nadler, F. Warner, and S. W. Zucker, Proceedings of the National Academy of Sciences 102, 7426 (2005).
- [37] B. Nadler, S. Lafon, I. Kevrekidis, and R. R. Coifman, in Advances in neural information processing systems (2006) pp. 955–962.
- [38] R. R. Coifman and S. Lafon, Applied and Computational Harmonic Analysis 21, 5 (2006), special Issue: Diffusion Maps and Wavelets.
- [39] Y. Michalevsky, R. Talmon, and I. Cohen, in Signal Processing Conference, 2011 19th European (IEEE, 2011) pp. 1299–1302.
- [40] O. Barkan, J. Weill, L. Wolf, and H. Aronowitz, in Proceedings of the IEEE International Conference on Computer Vision (2013) pp. 1960–1967.
- [41] V. Berezinskii, Sov. Phys. JETP 32, 493 (1971).
- [42] V. Berezinskii, Soviet Journal of Experimental and Theoretical Physics 34, 610 (1972).

- [43] J. M. Kosterlitz, Journal of Physics C: Solid State Physics 7, 1046 (1974).
- [44] W. P. Su, J. R. Schrieffer, and A. J. Heeger, Phys. Rev. Lett. 42, 1698 (1979).
- [45] A. Y. Kitaev, Physics-Uspekhi 44, 131 (2001).
- [46] Strictly speaking, this is not even necessary for the algorithm as it only requires calculating the kernel $K_{\epsilon}(x_l, x_{l'})$ evaluated at all samples.
- [47] We obtain the spectrum of P more efficiently by diagonalizing the similar matrix $A_{l,l'} = P_{l,l'} \sqrt{z_l/z_{l'}}$, which is symmetric and positive definite.
- [48] Y. Komura and Y. Okabe, Journal of the Physical Society of Japan 81, 113001 (2012).

SUPPLEMENT

S.1 Splitting between two topological sectors

In this section, we derive an expression for the splitting and wavefunctions of the leading (quasi)degenerate modes of $P_{l,l'}$ with $\lambda_k \simeq 1$ (i.e., of the zero modes in the language of the quantum-well problem). We discuss under which assumptions it is exponentially small and show that the algorithm is robust against an imbalance in the number of samples in different topological sectors.

For simplicity, let us focus on two topologically distinct sectors, denoted by A and B, respectively. This assumes low T so that both topological sectors are well-defined. As illustrated in Fig. 2(c), the kernel $K_{\epsilon}(x_l, x_{l'})$ has matrix elements of $\mathcal{O}(1)$ in the blocks with $l, l' \in A$ and $l, l' \in B$, but is of order $e^{-c/\epsilon}$ if $l \in A$, $l' \in B$ (or vice versa). The value of the order-1 constant c in the exponent depends on how strongly the two different sectors are separated with respect to the Euclidean norm in the definition of the kernel in Eq. (1).

As mentioned in the main text, we obtain the spectrum of $P_{l,l'}$ by first diagonalizing the matrix

$$A_{l,l'} = P_{l,l'} \sqrt{\frac{z_l}{z_{l'}}} = \frac{K_{\epsilon}(x_l, x_{l'})}{\sqrt{z_l} \sqrt{z_{l'}}}, \tag{S1}$$

which has the advantage of being symmetric. Being similar to P, it has the same spectrum as P and its eigenfunctions, denoted by $\bar{\psi}_k$ in the following, are related to ψ_k according to $(\psi_k)_l = (\bar{\psi}_k)_l/\sqrt{z_l}$. We now split the matrix A in Eq. (S1) into two parts, $A_{l,l'} = A_{l,l'}^{(0)} + A_{l,l'}^{(1)}$, where $A_{l,l'}^{(0)}$ is nonzero only if l and l' belong to the same topological sector. The matrix $A_{l,l'}^{(0)}$ has an eigenstate with eigenvalue of exactly one in each topological sector. The second part, and $A_{l,l'}^{(1)} = \mathcal{O}(e^{-c/\epsilon})$, will be treated as a perturbation which will lift the exact degeneracy.

To this end, we use $s \in \{A, B\}$ to label the two sectors and introduce the \bar{s} notation to indicate $\bar{s} = B$ for s = A (and vice versa). For $l \in s$, we write

$$z_l = z_l^s + \Delta z_l^s, \tag{S2}$$

where

$$z_l^s = \sum_{l' \in c} K_{\epsilon}(x_l, x_{l'}) = \mathcal{O}(1), \tag{S3a}$$

$$\Delta z_l^s = \sum_{l' \in \bar{s}} K_{\epsilon}(x_l, x_{l'}) = \mathcal{O}(e^{-c/\epsilon}).$$
 (S3b)

Within this notation, we have

$$A_{l,l'}^{(0)} = \frac{K_{\epsilon}(x_l, x_{l'})}{\sqrt{z_l^s} \sqrt{z_{l'}^s}}, \quad \text{for } l, l' \in s,$$
 (S4)

and $A_{l,l'}^{(0)} = 0$ if l, l' belong to different sectors. This matrix has an eigenvector with eigenvalues 1 for each sector s which is given by

$$(\bar{\psi}^s)_l = \begin{cases} \frac{\sqrt{z_l^s}}{\sqrt{\sum_{l' \in s} z_{l'}^s}}, & l \in s, \\ 0, & l \notin s. \end{cases}$$
 (S5)

The perturbation, $A^{(1)}$, consists of two parts — one which acts between different sectors, and a contribution resulting from the correction Δz_l^s to z_l^s . To leading order in $e^{-c/\epsilon}$, we find

$$A_{l,l'}^{(1)} \sim \begin{cases} -\frac{K_{\epsilon}(x_{l}, x_{l'})}{2\sqrt{z_{l}^{s}}\sqrt{z_{l'}^{s}}} \left(\frac{\Delta z_{l}^{s}}{z_{l}^{s}} + \frac{\Delta z_{l'}^{s}}{z_{l'}^{s}}\right), & l, l' \in s, \\ \frac{K_{\epsilon}(x_{l}, x_{l'})}{\sqrt{z_{l}^{s}}\sqrt{z_{l'}^{s}}}, & l \in s, l' \in \bar{s}. \end{cases}$$
(S6)

Given the explicit form of the unperturbed states in Eq. (S5) and of the perturbation (S6), it is straightforward to perform degenerate perturbation theory. One finds

$$\lambda_0 = 1, \tag{S7a}$$

$$\lambda_1 = 1 - M_{AB} \left(\frac{1}{M_{AA}} + \frac{1}{M_{BB}} \right) + \mathcal{O}(e^{-2c/\epsilon}), \quad (S7b)$$

where we have defined

$$M_{ss'} = \sum_{l \in s} \sum_{l' \in s'} K_{\epsilon}(x_l, x_{l'}). \tag{S8}$$

The associated wavefunctions read as

$$\bar{\psi}_0 = \mathcal{N} \left(\eta \, \bar{\psi}^A + \bar{\psi}^B \right), \quad \eta = \sqrt{M_{AA}/M_{BB}}, \quad (S9a)$$

$$\bar{\psi}_1 = \mathcal{N} \left(\bar{\psi}^A - \eta \, \bar{\psi}^B \right) \tag{S9b}$$

with normalization factor \mathcal{N} .

First, note that the larger eigenvalue, λ_0 , is still 1 which, in fact, must hold to all orders in perturbation theory as a result of global probability conservation, $\sum_{l'} P_{l,l'} = 1$. As expected, the associated eigenstate, $\bar{\psi}_0$, is the symmetric superposition of the two eigenstates, $\bar{\psi}^A$ and $\bar{\psi}^B$, found by first considering the topologically distinct sectors separately. Because $M_{AB} = \mathcal{O}(e^{-c/\epsilon})$, the eigenvalue of the antisymmetric combination $\bar{\psi}_1$ is

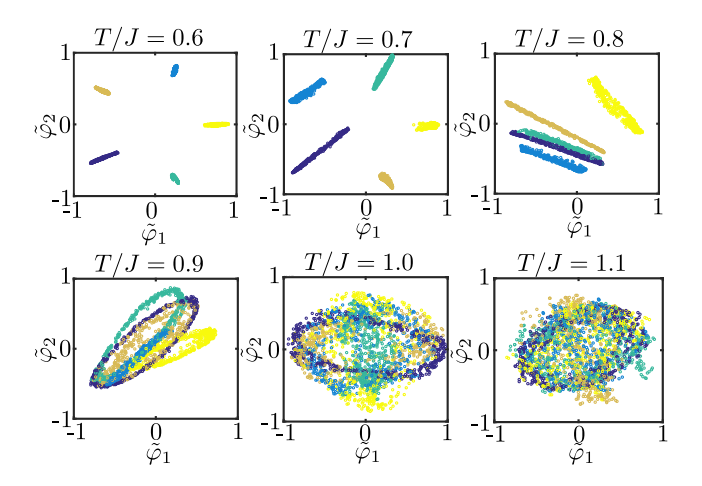


Figure S1. Projection of the 4-dimensional reduced feature space, Eq. (7) of the main text, on a two-dimensional plane for increasing values of T/J. The color code refers to the winding number of each sample.

reduced from one by an exponentially small amount, see Eq. (S7b). More precisely, this splitting scales as

$$1 - \lambda_1 \propto e^{-c/\epsilon} \left(\frac{m_A}{m_B} + \frac{m_B}{m_A} \right), \tag{S10}$$

with ϵ and the number of samples m_s in sector s. Consequently, as long as the asymmetry ratio $R = \max(\frac{m_A}{m_B}, \frac{m_B}{m_A})$ is smaller than the exponential scale $e^{c/\epsilon}$, the perturbative approach presented here is valid. In this case, the quasi-degenerate eigenstates should be clearly visible in the spectrum of the diffusion map, and deviations from degeneracy scale exponentially with ϵ .

We finally mention that the weak requirement $R \ll e^{c/\epsilon}$ can be further relaxed by proper rescaling of the kernel. Using (this corresponds to $\alpha=1$ in the notation of Ref. 38) the kernel

$$K_{\epsilon}(x_l, x_{l'}) = \frac{\exp\left(-\frac{||x_l - x_{l'}||^2}{2N\epsilon}\right)}{n_{\epsilon}(x_l)n_{\epsilon}(x_{l'})},$$
 (S11a)

$$n_{\epsilon}(x_l) = \sum_{l'} \exp\left(-\frac{||x_l - x_{l'}||^2}{2N\epsilon}\right), \quad (S11b)$$

instead of the kernel in Eq. (1), the factors m_A/m_B and m_B/m_A in the scaling (S10) of the eigenvalue will be eliminated at order $e^{-c/\epsilon}$. We have checked that the BKT transition can be equally well detected (yielding the same T_c within the accuracy of our simulations) with the kernel in Eq. (S11).

S.2 Applying k-means to the reduced feature space φ

To classify the samples, we use the k-means algorithm, which is a standard clustering algorithm for unsupervised machine learning [1, 2]. In our case, each sample x_l has an associated (n-1)-dimensional feature vector $\varphi_l = [(\psi_1)_l, \ldots, (\psi_{n-1})_l]$, see Eq. (7) in the main text, formed by the largest degenerate eigenvectors of the transition matrix $P_{l,l'}$. As already discussed in the main text, the zeroth eigenvector, $(\psi_0)_l$, which has the same components for all samples, is not useful for labeling purposes.

The goal of k-means is to partition the m samples into k subsets S_j , $j = 1, \ldots, k$, in order to minimize the function

$$\mathcal{F} = \min \left[\sum_{j=1}^{k} \sum_{l \in S_j} ||\varphi_l - \mu_j||^2 \right], \quad (S12)$$

where μ_j is the center of mass of subset S_j . Once Eq. (S12) is minimized, each sample $x_l \in S_j$ is given the label j. As follows from our discussion of the main text, we use k = n as the number of clusters to classify samples according to their topological properties.

S.3 Clustering across the BKT transition

In this section, we extend the results of Fig. 3(d) to illustrate in more detail how the clustering of the samples fails as the phase transition is approached. Figure S1 shows the projection of the low-dimensional feature space, Eq.(7) in the main text, into a two-dimensional plane that has been optimized to make the clustering clearly visible. For $T/J \leq 0.6$, samples are tightly clustered by topological sector. In the range, T/J = 0.7-0.8, clusters are still well defined, but they start to merge. For $T/J \geq 0.9$, the clusters merge into a single cluster; topological sectors are no longer well defined, which is the defining feature of the topological phase transition.